



Pergamon

Available online at www.sciencedirect.com

SCIENCE @ DIRECT®



www.actamat-journals.com

Acta Materialia 51 (2003) 5359–5373

Direct in situ measurements of bridging stresses in CFCCs

Konstantinos G. Dassios^{a,b,c,*}, Costas Galiotis^a, Vassilis Kostopoulos^{a,b},
Marc Steen^c

^a *Foundation of Research and Technology Hellas, Institute of Chemical Engineering and High Temperature Processes, Stadiou Street, Platani, Patras GR-26504, Greece*

^b *Department of Mechanical Engineering and Aeronautics, University of Patras, Rio GR-26500, Greece*

^c *Institute for Energy, Joint Research Centre, European Commission, Westerduinweg 4, 1755 LE Petten, The Netherlands*

Received 11 April 2003; accepted 12 July 2003

Abstract

The macro- and micro-mechanics of large scale bridging in SiC/MAS-L composites were assessed by tensile testing of DEN specimens with in situ LRM measurements. The macromechanical behavior was analyzed in terms of crack growth resistance and bridging laws using an elastic displacement correction approach. A dedicated Raman calibration curve was established for the specific composite fiber, which served in the transformation of wavenumber shifts collected from bridging fibers in the composite to bridging strain, and to stress via the elastic modulus of the fibers. Bridging strain profiles were established along the ligament of the specimen and their shape was discussed in conjunction with local notch effects. Actual bridging strain values up to 0.8% were calculated which compared well with their macromechanical counterparts within the intact-fiber regime. The individual contributions of intact and pulled-out fibers to the total fracture behavior of the composite were distinguished and are discussed in the article.

© 2003 Acta Materialia Inc. Published by Elsevier Ltd. All rights reserved.

Keywords: Tension test; Raman spectroscopy; Ceramic matrix composites (CMC); Fiber reinforced composites; Fracture

1. Introduction

The development of ceramic composites reinforced by particulates, whiskers or fibers overcomes the fundamental problem of inherent brittleness that has been limiting the use of monolithic ceramics in structural engineering applications for many years. It is now well established that, of all

the types of reinforcement, continuous ceramic fibers provide a ceramic with the greatest increase in fracture toughness and damage resistance. The enhanced damage resistance and increased fracture toughness of continuous fiber-reinforced ceramic matrix composites (CFCCs) is due to their inherent ability to effectively redistribute stresses around holes, notches and cracks, a phenomenon which stems from the development of shielding forces in the process zone around the crack tip.

With the exception of Class III composite fracture, where the process zone consists of multiple unordered shear matrix microcracks in front of the

* Corresponding author. Tel.: +30-261-096-5277; fax: +30-261-096-5223.

E-mail address: cdassios@mech.upatras.gr (K.G. Dassios).

crack tip, fracture in the vast majority of CFCCs is associated with the formation and propagation of macrocracks (Class I and Class II fracture) [1]. The corresponding process zone consists of two parts: the so-called bridging zone with fiber bridging and pull-out developing within the macrocrack and a matrix cracking process zone ahead the macrocrack. The increase in fracture resistance is a result of several energy-dissipating mechanisms acting in the two zones. In the matrix process zone, a complex set of phenomena such as matrix microcracking, fiber/matrix interfacial debonding and transformation toughening may take place concurrently. In the bridging zone, the cracked matrix is bridged by intact and/or failed fibers, which debond, slip and pull-out. The role of the bridging zone in the fracture resistance of the composite is of particular importance as the bridging fibers carry a significant portion of the applied load, hence resisting further crack opening.

When the dimensions of the bridging zone are comparable to any specimen dimension—a phenomenon known as large scale bridging (LSB) encountered in most CFCCs—the well established rising crack growth resistance with increasing crack extension behavior of the composite (*R*-curve) is a material-extrinsic property which depends upon specimen geometry and dimensions [2,3]. Under LSB conditions, the fracture behavior of CFCCs is preferably characterized by means of a bridging law, a local correlation between the stresses developing in the fibers within the bridging zone (bridging stresses) and the crack opening displacement (COD), i.e. the local opening of the crack flanks. The bridging law concept is a measure of the crack closure traction normalized to the local geometrical and dimensional characteristics of the material and, as such, has been proposed to serve as a basic, intrinsic, material law [4]. A number of studies have focused on the measurement of macromechanical bridging laws for composite materials mainly through the calculation of the bridging stress from the *R*-curve behavior of the material [4–11]. Rouby and colleagues [12] proposed a straightforward procedure for the macromechanical evaluation of bridging stresses and bridging laws in double-edge notch (DEN) composite specimens based on the deconvolution of the

load-displacement behavior into an intact/bridging fiber and a pull-out fiber contribution.

While the macromechanical quantification of bridging stresses and laws in CFCCs has been studied intensively over the last years, our knowledge of the micro-mechanisms active in the bridging zones of such materials is still very limited; for example, currently, there do not exist measured values of the loads or stresses carried by bridging fibers at the microscale. The current limitation arises mainly from the fact that macromechanical testing can, by definition, only provide information on the composite as a “closed system” where the contributions of the different phases of the composite to the total recorded behavior cannot be valued independently except through the use of specific assumptions. Most current theoretical models, phenomenological or analytical, suffer from lack of experimental verification and, hence, can only provide semi-quantitative estimates of the actual performance. As a result, the current macromechanically established bridging stresses and laws for various composite materials have overlooked the effects of active internal micro-mechanisms, such as variations within the reinforcing phase, interphasial/interfacial effects, inhomogeneities in volume fraction and porosity, interactions between the composite phases, and other factors that can bias the calculated bridging stresses. The development of straightforward techniques that quantify the individual contribution of the reinforcing phase in the overall composite behavior, that provide a comprehensive understanding of the true bridging loads and stresses active within the bridging zone, and that validate the current macromechanical models and findings, appears to be a unique need.

While the mechanical testing of full composites provides representative data on their properties and their macroscopical performance when used in structures, diffraction and spectroscopic techniques can provide information on the micromechanics that govern the load transferring mechanisms, the stress singularities and their fracture behavior. The high spatial resolutions and large penetration depths associated with laser raman microscopy (LRM) have established this technique as the only experimental method to date for assessing the

micromechanics of deformation of ceramic fibers at the microscale. LRM enables the determination of stresses and strains in fibers with a spatial resolution of 1 μm and can be used to directly measure important micromechanical parameters that have traditionally been obtained using indirect and experimentally delicate methods. The principle of the LRM technique, the Raman effect, is associated with the inelastic scattering of light by the molecules of a material. The Raman spectrum contains characteristic peaks at frequencies corresponding to the specific vibrational modes of the scattering molecules in the material. The application of a mechanical or thermal strain field, leads to the alteration of interatomic distances between the molecules and, hence, to a change in their vibrational modes [13], an effect which appears in the Raman signal in the form of wavenumber shifts of the characteristic vibrational frequencies from their stress-free position. The Raman effect is particularly apparent in crystalline materials that immediately transfer the macroscopically applied stress to the atomic bonds. Most reinforcing fibers are crystalline and, therefore, have been found to exhibit this effect. The wavenumber shifts of Raman peaks from the stress-free value are indicative of the mechanical response of fibers to externally applied deformation. Owing to the shape of the interatomic bond well, a tensile strain field causes the Raman peaks to shift to lower wavenumbers, whereas compressive strain has the opposite effect. The LRM technique has been successfully applied in the past for micro-strain measurements in model carbon/epoxy [14–16] and aramid/apoxy composites [17–19], as well as in real systems such as SiC/Osumilite glass ceramic composites [20].

In this study, the LRM technique is applied for the in situ quantification of strain in SiC fibers in the bridging zone developing during the testing of DEN SiC/MAS-L specimens. Initially, the magnitude of Raman wavenumber shifts of the fibers from their stress-free position was calibrated against externally applied strain by loading individual SiC fibers extracted from the composite in axial tension in order to derive the fiber-specific Raman calibration curve. The inverse methodology was applied for the evaluation of bridging strain in

the composite: the frequency shifts in the Raman spectra collected from bridging fibers that were present between matrix macrocracks during testing were converted to strain via the established calibration curve.

The scope of this study is to demonstrate the potential of the LRM technique when applied in full CFCCs, especially for the in situ assessment of deformation in the reinforcing phase. It also aims to provide a real measure of strains and stresses developing within the bridging fibers during fracture of a SiC/MAS-L composite and to demonstrate differences between experimentally determined bridging strains at the microscale and values derived from macromechanical models based on the analysis of the *R*-curve behavior of CFCCs [21,22].

2. Background

2.1. Fiber bridging of macrocracks

The mechanical behavior of a fiber-bridged crack has been studied extensively in the past [23–26]. The Class I fracture characteristics (formation and development of a single macrocrack) of a brittle-matrix fiber-reinforced composite are presented in the load–displacement (*F*–*d*) behavior of Fig. 1a, whereas the mechanical processes occurring during testing are schematically depicted in Fig. 1b. During the initial loading stages, reversible mechanical phenomena occur within the composite (region O→A in Fig. 1a, stage 2 in Fig. 1b). The first matrix crack (point A in Fig. 1a) triggers the appearance of the bridging zone while cracking evolves (region A→B in Fig. 1a, stage 3 in Fig. 1b) until the macrocrack has fully developed, spanning the total width of the specimen (point B in Fig. 1a, stage 4 in Fig. 1b). Beyond this stage, fibers start failing within the volume of the composite and the load-carrying capacity of the remaining fibers decreases until a critical number of fibers have failed (point C in Fig. 1a). Failed fibers undergo pull-out and an additional contribution to the recorded load arises, owing to friction at the fiber/matrix interface (region B→D in Fig. 1a, stage 5 in Fig. 1b). Under the global load-sharing

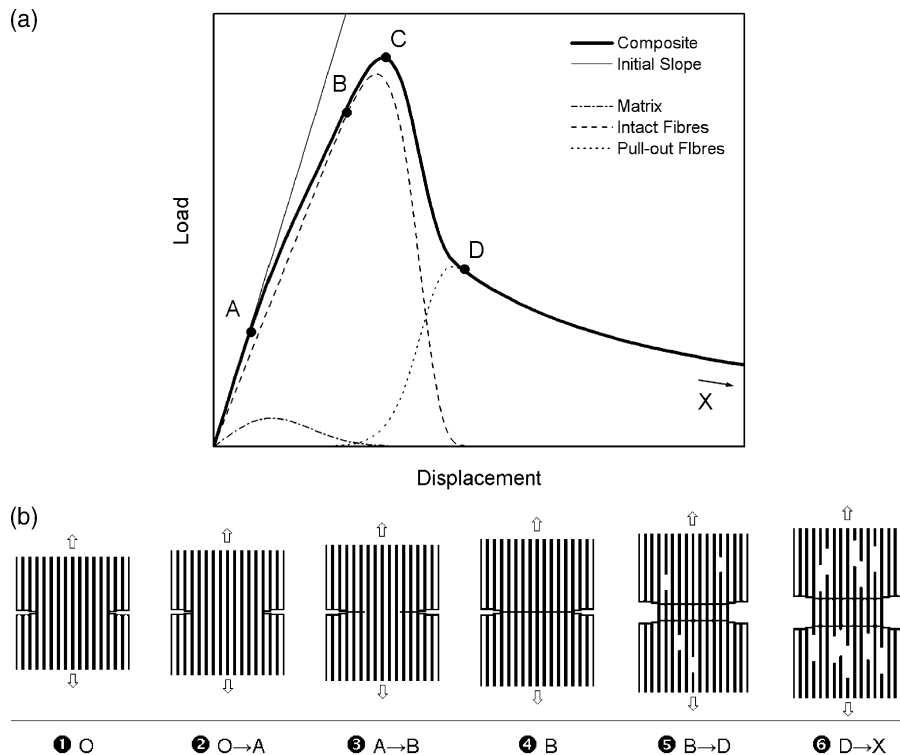


Fig. 1. (a) Load–displacement (F – d) curve typical of Class I composite fracture and deconvolution of the curve into fiber and matrix contributions. (b) Schematic overview of the main fracture processes in the composite.

principle, each fiber failure is followed by a uniform redistribution of the remaining load to the surviving fibers. As the portion of load that corresponds to each intact fiber is greater after the redistribution, more failures are induced and the process evolves until all fibers have failed (point D in Fig. 1a). Beyond this stage, the load carried by the composite corresponds entirely to interphasial friction due to pull-out of the failed fibers (region D→X in Fig. 1a, stage 6 in Fig. 1b). With increasing displacement, the fiber ends that were originally located at various statistical locations inside the composite are sequentially disengaged from the matrix until, eventually, the composite separates in two parts.

In summary, the main mechanisms typical of Class I composite behavior are, in order of appearance: linear elastic composite behavior (O→A), linear elastic fiber behavior (A→B), crack bridging by intact and pulled-out fibers (B→D) and purely frictional bridging due pull-out of the failed fibers

(D→X). Accordingly, the corresponding F – d curve of the composite is the sum of three individual contributions (Fig. 1a): A limited contribution corresponding to the load carried during the early loading stages by the fibers and the brittle matrix, a contribution corresponding to the load carried by the surviving fibers—which can be assumed identical to that of a fiber bundle where load is carried by a large number of fibers acting independently and a contribution corresponding to friction by fiber pull-out.

2.2. Calculation of crack opening

In extension controlled tests, the externally applied energy is consumed in reversible and irreversible phenomena and, accordingly, the total displacement is equal to the sum of a linear and a non-linear contribution. In Class-I fracture, the non-linear part of the total displacement corresponds exclusively to crack opening, i.e. separation

of the opposite sides of the macrocrack which, in turn, is always associated with the presence of a bridging zone. For example, in the regime beyond the fully developed macrocrack (beyond point B in Fig. 1a), the load carried by a DEN specimen is equal to that carried by the bridging (either intact or failed) fibers, F_{br} . Hence, the crack opening can be calculated by subtracting the elastic displacement of the system from the total recorded displacement, d . If D_0 is the initial slope of the measured load–displacement curve, the crack opening, $e(d)$, is obtained from the instantaneous load–displacement pairs (F, d) through:

$$e(d) = d - \frac{F(d)}{D_0} \tag{1}$$

Fig. 2 is a graphical illustration of the elastic displacement correction corresponding to Eq. (1).

2.3. Crack growth resistance curve and bridging stresses

Accepting that non-linear contributions to the measured displacement stem directly from the presence of the bridging zone, the bridging work that contributes to the increase of crack opening

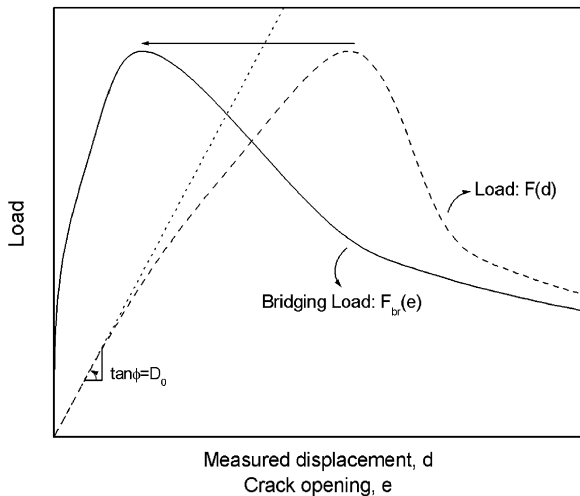


Fig. 2. Conversion of the measured load–displacement curve to a bridging load–crack opening curve using elastic displacement correction.

resistance can be calculated as the area under the bridging stress vs. crack opening curve (Fig. 3):

$$\Delta R = \Delta G = \int_0^e \frac{F_{br}(e)}{t \cdot (w - 2\alpha_0)} \cdot de \tag{2}$$

In Eq. (2), t is the specimen thickness, α_0 is the notch width and $t \cdot (w - 2\alpha_0)$ represents the area of the bridging zone, i.e. the cross-section of the bridged ligament of the specimen. Accordingly, the integrand in Eq. (2) represents the nominal bridging stress, $\sigma_{br}(e)$.

$$\sigma_{br}(e) = \frac{F_{br}(e)}{t \cdot (w - 2\alpha_0)} \tag{3}$$

Eq. (3) represents the directly measured (real) bridging law.

3. Materials, specimens and testing

The material used in this study is a laminated cross-ply SiC/MAS-L composite processed by EADS (ex-Aérospatiale, France). The reinforcing SiC fibers are grade Nicalon NL202 with a chemical composition in weight concentration terms of 56.6% Si, 31.7% C and 11.7% O. The main properties of the SiC–Nicalon fiber, as reported by the manufacturer, Nippon Carbon Co. Ltd., are presented in Table 1.

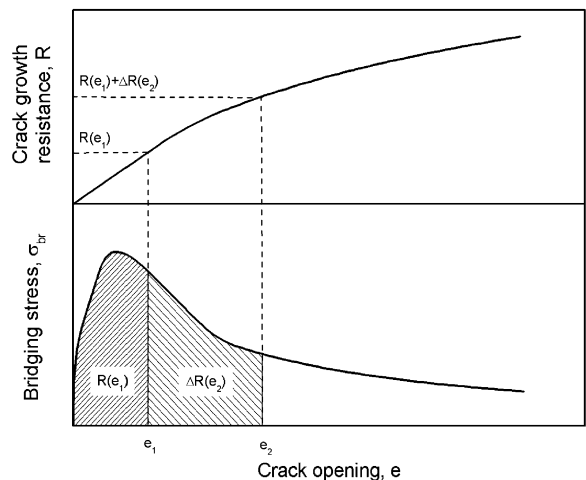


Fig. 3. DEN specimens: evaluation of the R -curve from the bridging load–crack opening curve.

Table 1
Typical properties of silicon carbide–grade Nicalon NL202 fibers

Property	Value
Filament diameter (μm)	12–14
Tensile strength (GPa)	3.0
Tensile modulus (GPa)	220
Failure strain (%)	1.4
Weibull modulus (25 mm g.l.)	3
Density (g/cm^3)	2.55
Coefficient of thermal expansion ($10^{-6} \cdot ^\circ\text{C}^{-1}$)	3.9 (25–500 $^\circ\text{C}$)
Specific heat ($\text{J} \cdot \text{g}^{-1} \cdot ^\circ\text{C}^{-1}$)	0.71 (25 $^\circ\text{C}$) 1.17 (500 $^\circ\text{C}$)

The glass–ceramic matrix contains MgO , Al_2O_3 , SiO_2 and LiO_2 and is made via the sol–gel route. Plates of 2.0 and 3.0 mm thickness with 8 and 12 plies respectively were produced via hot pressing. The laminae were stacked together in a symmetric $[0-90^\circ]_{2s}$ and $[0-90^\circ]_{3s}$ orientation for the 2.0 and 3.0 mm thick plate, respectively. The effective volume fraction of the fibers in the loading direction is 0.17 [12], whereas the matrix stiffness (75 GPa) and failure strain are lower than the corresponding values for the fiber and hence cracks appear first in the matrix.

Double edge notch specimens of 2.0 and 3.0 mm thickness were machined from the corresponding composite plates using a $150 \mu\text{m}$ thick diamond disk so that the external plies were oriented parallel to the tensile direction (0°). Typical double edge notch specimens used in this study are presented schematically in Fig. 4. Specimens with 0.4, 0.5 and 0.6 initial notch-to-width ratios were produced using a diamond disk of the same thickness, while the specimen width, W , was 12 mm for the 2 mm thick specimens and 10 mm for the 3 mm thick specimens.

Mechanical testing under monotonic tensile loading conditions was performed in extension control on an MTS® 858 servo-hydraulic tabletop equipped with a 25 kN load cell under a constant cross-head velocity of 0.01 mm/min. Displacement was measured directly on the specimens by fixing an MTS® axial extensometer (gauge length 25 mm) to one side. A typical load–displacement curve obtained for a 3 mm thickness specimen with an initial notch-to-width ratio of 0.5 is presented in Fig. 5. In this figure, the hollow circles represent

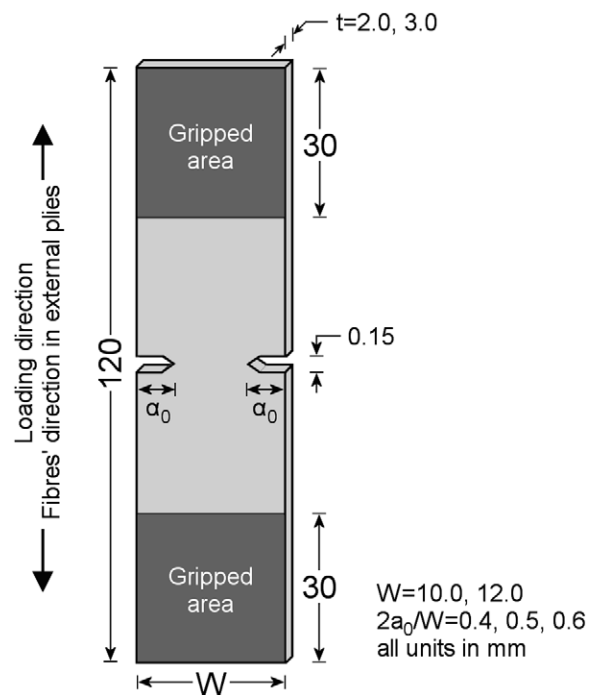


Fig. 4. Dimensional characteristics of the DEN C/C specimens (nominal values).

the experimental data, whereas the solid lines are theoretical predictions of the matrix (M), fiber (F) and pull-out (P) contributions to the total recorded behavior. For the matrix and fiber, the behavior has been approximated using 2-parameter Weibull distributions, whereas the pull-out contribution was a modified Weibull function. A regression of the sum of the three contributions was performed under the chi-square reduction criterion on the basis of the analysis presented in [27,28], where

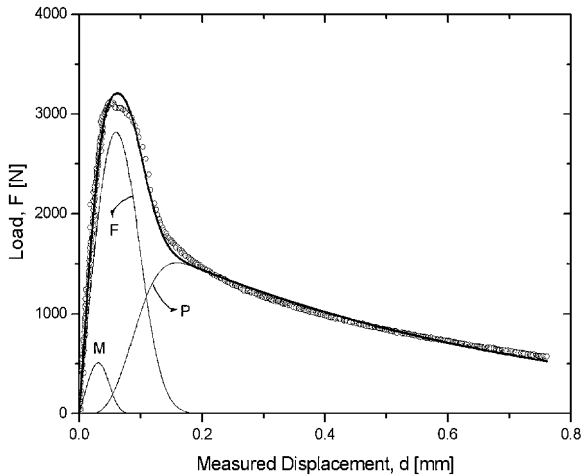


Fig. 5. Typical load–displacement curve for a DEN specimen under monotonic tensile loading.

the fundamentals of using Weibull statistics to analytically predict the bridging contributions of intact and pull-out fibers are discussed. The predicted behavior (thick solid line in Fig. 5) approximates well the experimental data and a Weibull modulus of 2.7 was estimated for the fibers, which is accordance with other studies [29,30].

4. Experimental procedure for in situ Raman measurements

4.1. Spectroscopic setup

A schematic of the complete experimental setup used for the direct in situ measurement of bridging stresses during composite testing is presented in Fig. 6. The spectroscopic system consists of a newly developed compact Remote Raman Microscope (Galiotis et al., “ReRaM System III”) with an integrated Argon-ion laser source. The monochromatic excitation radiation has a wavelength of 514.5 nm. The Raman microscope is attached to a 3-D translational stage with step-motion ability of 1 μm in each direction positioned in front of the MTS® mechanical testing frame. Both frame and microscope rest on a vibration-free table. The monochromatic laser radiation is polarized in the direction of the loading axis, parallel also to the

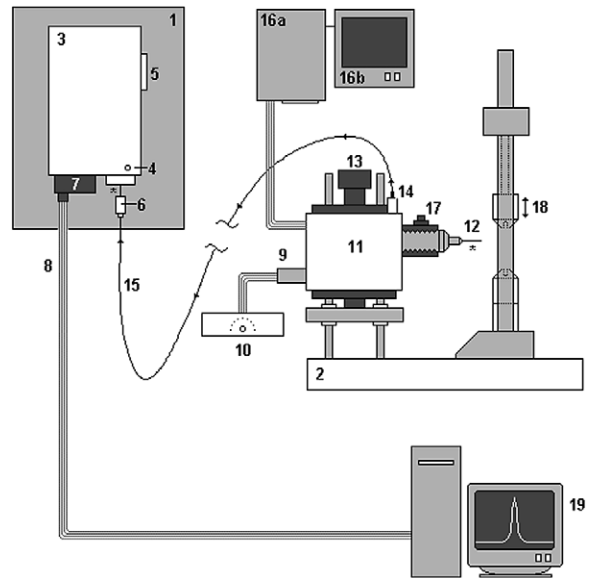


Fig. 6. The ReRaM/mechanical testing setup (Galiotis et al., “ReRaM System III”). 1 and 2. Vibration-free tables, 3. Spectrometer, 4. Aperture control, 5. Frequency window selection, 6. Fiber optic alignment receptor, 7. CCD detector, 8. CCD data acquisition, 9. Argon-ion laser source, 10. Laser power control, 11. Raman microscope, 12. Objective lens, 13. XYZ micro-translational stage, 14. Collection output, 15. Collection fiber optic, 16. Video recorder (a) and display (b), 17. Observation light source, 18. MTS Servo-hydraulic frame, 19. Raman spectra processing.

orientation of the bridging fibers (0°). High-performance polarization-preserving fiber optics are used to collect and transfer the Raman signal to the remote spectrometer (SPEX® 1000M Single Monochromator). Using an objective lens with a $\times 50$ magnification power, a laser spot of 4–5 μm in diameter is achieved which corresponds to ca. 1/3 of the diameter of the target fiber. At that spot size level, an incident laser power of 2.6 mW and an integration time of 20 s were found to be the optimal combination of parameters for use with the specific fiber as they do not produce local thermal energy accumulation on the fiber surface; a process which can lead to undesirable shifts in the Raman signal. These values were selected following a parametric investigation of the effect of laser power and integration time to the stress-free position of the Raman line of the SiC fiber.

4.2. Raman calibration curve for the SiC–Nicalon fiber

Raman spectra were initially obtained from individual as-received SiC–Nicalon fibers originating from a tow (Nippon Carbon Co. Ltd., Japan), as well as from stress-free mono-filaments extracted from a composite using an alcohol dispersion technique. The spectra show two prominent bands at 1350 and 1675 cm^{-1} which correspond, respectively, to the A_{1g} and E_{2g} modes of graphite in the fibers. Typical spectra of the as-received and extracted fibers are shown in Fig. 7.

Although the bands appear in the same position for both as-received and extracted fibers, the significant line-broadening in the spectrum of the as-received fiber as compared to the sharper and much better defined lines obtained from the extracted fiber suggests that the fibers in the composite have undergone significant graphitization, apparently during hot-pressing of the plates. The graphitization level of carbon-containing fibers is directly associated with their mechanical properties—for example, a higher graphitization level corresponds to a higher elastic modulus. Given this fact, and in order to derive a Raman calibration curve that will representatively translate wavenumber shifts of fibers in the composite into strain, calibration was performed on SiC mono-filaments extracted from the composite instead of the as-received fibers.

Single extracted fibers of length of ca. 30 mm were bonded to conventional paper “window” tabs

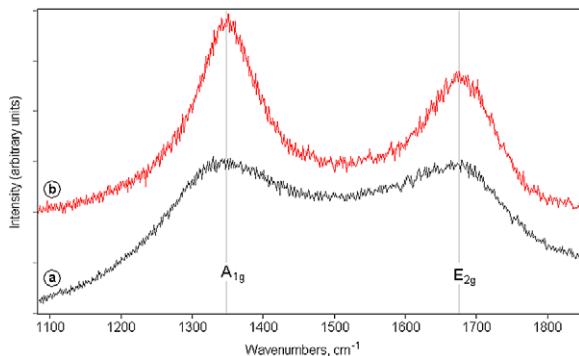


Fig. 7. Raman spectra obtained from stress-free SiC–Nicalon fibers: (a) as-received condition and (b) extracted from the SiC/MAS-L composite.

that provide an effective gauge length of 10 mm and were tested in monotonic axial tension on a custom micro-extension base. The fibers were subjected to monotonic displacement that was applied sequentially with a step of 20 μm or an equivalent strain step of 0.2%. Using the spectroscopic setup presented in the previous section, three Raman spectra were collected at each extension level on the same position on the fiber at the middle of the gauge length. The dependence of the 1350 cm^{-1} band position on tensile strain is presented in Fig. 8. A linear relation between the 1350 cm^{-1} band position and the fiber strain is observed and the shift rate is 7.5 cm^{-1} per percent of applied strain with a standard deviation of 0.29 cm^{-1} . Fiber failure occurred at approximately 1.3% applied strain.

4.3. In situ Raman measurements

During monotonic tensile testing of double edge notched SiC/MAS-L specimens, the outer surface of the specimen (0° ply) was constantly monitored through the Raman microscope by using a low magnification ($\times 4$) lens focusing along the ligament between the notches. Shortly after the application of load, matrix microcracks form and

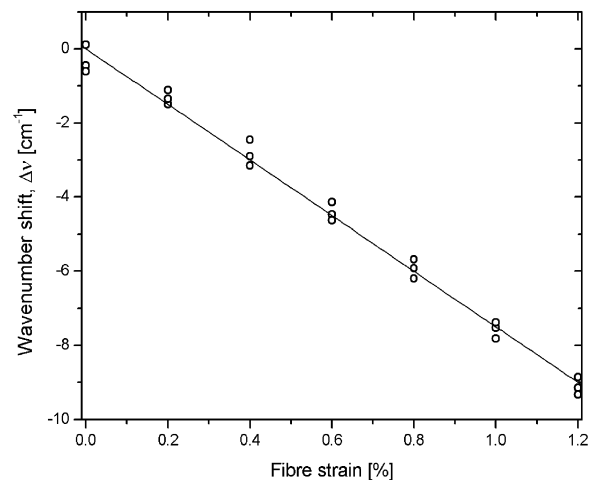


Fig. 8. The strain-based Raman calibration curve obtained for a graphitized SiC–Nicalon fiber extracted from the composite. The y-axis represents the difference of the 1350 cm^{-1} band position from its stress-free value. Hollow circles represent experimental data, whereas the solid line represents the linear fit to the data.

develop at both notch roots at random vertical positions. The microcracks are oriented normal to the direction of loading and, with increasing load, propagate within the matrix towards the facing notch. The phenomenon evolves until a critical crack density is established where the different paths of adjacent microcracks merge to form a dominant, fully developed macrocrack that spans the width of the ligament. Upon the formation of a fully developed macrocrack, the remaining microcracks do not propagate further. In the bridging zone, bridging fibers stretch, fail in the matrix and pull-out. The bridging phenomenon is particularly prominent for the material tested in this study. The pull-out contribution was also extensive owing to a weak fiber/matrix interface. The fully developed macrocrack reveals a vast amount of bridging fibers on the external surface of the composite, which serve as collection sites for the Raman microprobe. A microscope picture of the bridging zone obtained during testing gives an impression of the extent of bridging (Fig. 9).

After the development of the dominant macrocrack and the appearance of bridging, the extension-controlled procedure was systematically paused (extension hold) and the Raman spectra were collected from individual fibers within the bridging zone (Fig. 9c) by increasing the resolution of the microscope to a $\times 50$ magnification in order to accurately focus the Raman microprobe on the surface of a single fiber. At each extension level, the spectra were collected on 100 bridging fibers at equally spaced locations along the ligament. For each fiber, three spectra were collected on different positions along its length in order to obtain a statistical measure of the measurement.

5. Results and discussion

5.1. Macromechanical analysis

The bridging stress is calculated as a function of crack opening directly from the bridging load using Eq. (3) and is presented in Fig. 10 for DEN specimens with three different notch-to-width ratios and for two distinct specimen thicknesses. As discussed in a previous section, the macroscopical bridging

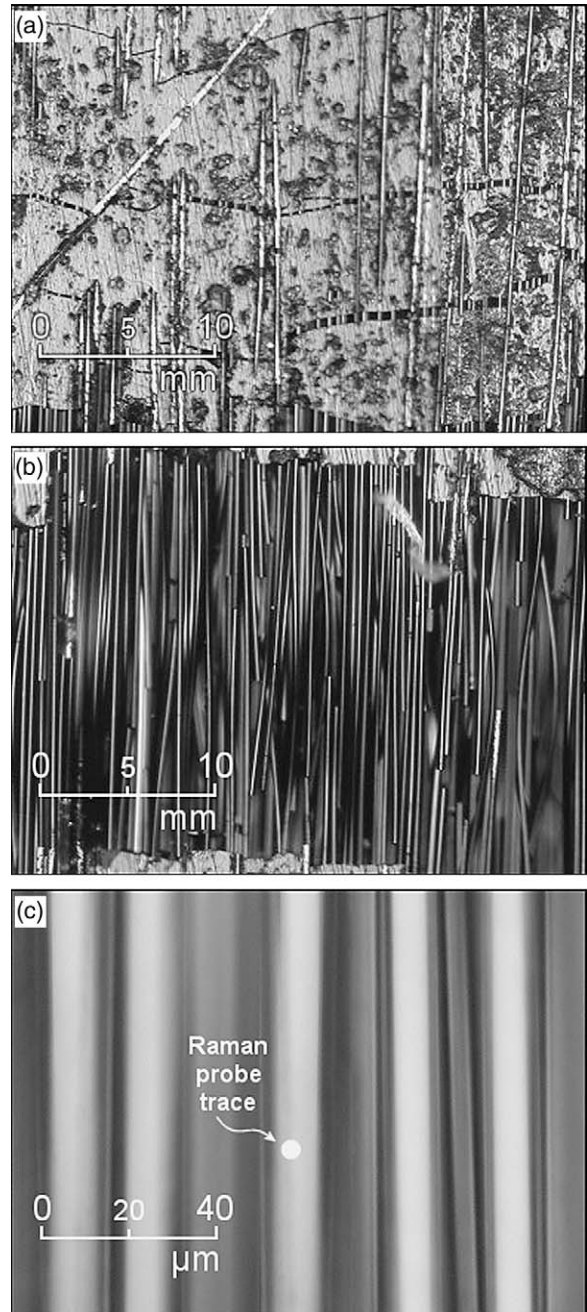


Fig. 9. Large scale bridging in SiC/MAS-L composite: In situ microscopical damage observation during testing. Magnifications: (a) matrix microcracking during the early fracture stages, (b) fiber bridging and pull-out and (c) typical resolution window of the LRM measurements.

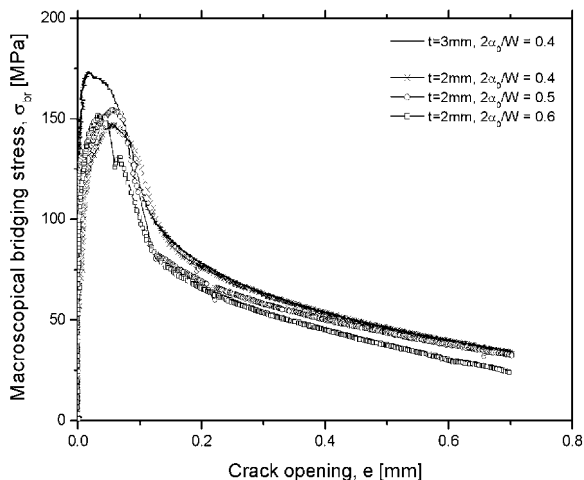


Fig. 10. SiC/MAS-L composite: Directly measured bridging laws for different notch dimensions.

stress is composed of two individual contributions, namely stress carried by (a) intact bridging fibers and (b) failed fibers through friction at the interface.

The data in Fig. 10 imply that the magnitude of bridging stresses depends on specimen thickness. The 3 mm thick specimen attains a maximum bridging stress value of 175 MPa, whereas the corresponding value for the 2 mm thick specimens is of the order of 150 MPa. For the thinner specimens, no apparent relation is noted between the maximum bridging stress and the notch length. On the other hand, a relation between notch length and the shape of the bridging law is apparent. In particular, the bridging stress profile decays more rapidly in specimens with higher notch-to-width ratios compared to those with larger ligament cross-sectional areas.

The rising part of the bridging profile corresponding to the development of the macrocrack is smoother for thinner specimens in contrast to the behavior of thicker specimens, where the macrocrack appears to occur shortly after first matrix cracking. Accordingly, the maximum bridging stress is attained at larger crack openings for thinner specimens. The contribution of intact fibers to the measured bridging stress profile is confined to the same crack opening regime of 0–0.12 mm for all the specimens, whereas a well-defined pull-out

regime commences beyond that crack opening. Given the fact that the specimen length is fixed, then, the level of strain experienced by the fibers within the bridging zone is the same at each crack opening, independent of the specimen geometry. Thus, the transition point from intact-to-pull-out fiber bridging is expected to be the same for all the specimens.

The energy consumed by the bridging zone as resistance to further crack opening is calculated for each crack opening increment using Eq. (2) and the findings are summarized in Fig. 11 which presents the total crack growth resistance R which is the sum of the initial crack growth resistance R_0 and bridging contribution ΔR . For the SiC/MAS-L composite, the initial crack growth resistance is very small (0.1–0.2 kJ/m², [12]) due to the very brittle glass–ceramic matrix and it is not visible in the scale of Fig. 11. The slopes of the R -curves decrease at a crack opening of 0.12 mm manifesting the higher crack growth resistance potential of the intact fibers as compared to the failed fibers undergoing pull-out.

5.2. LRM measurements

The Raman spectra were analyzed in terms of wavenumber shifts of the 1350 cm⁻¹ band position from its stress-free position. The exact position of

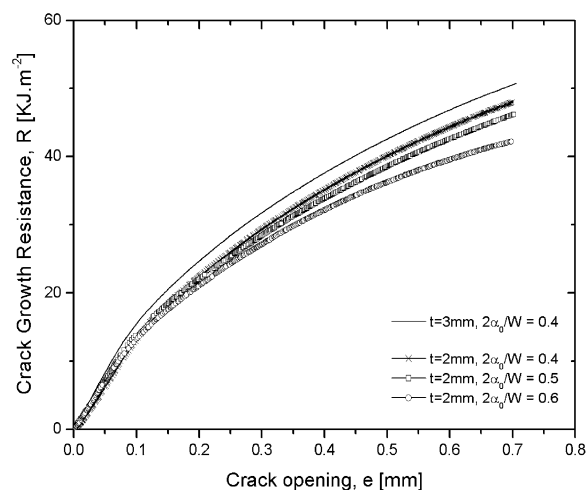


Fig. 11. SiC/MAS-L composite: Crack growth resistance curves for different thickness and notch lengths.

the stress-free 1350 cm^{-1} band was determined after the end of the test, while the specimen was stress-free, by collecting 50 Raman spectra on the free standing tips of equal in number pulled-out fibers. The standard deviation of the stress-free position of the 1350 cm^{-1} band, 0.38 cm^{-1} , represents the accuracy of the Raman measurements. The wavenumber shifts were converted to fiber strain using the Raman calibration curve (Fig. 8). These calculated strains correspond to net local strains that individual fibers in the bridging zone are subject to during testing. On the other hand, the strain measured by the extensometer (symmetrically positioned around the notch) is the sum of two components: (i) the notched/bridging zone and (ii) the un-notched region of the composite within the 25 mm gauge length. As discussed in a previous section, after the development of the macrocrack, the source of any non-linear displacement emanates only from crack opening within the bridging zone, whereas the un-notched region of the composite within the 25 mm gauge length displaces linearly. One could then evaluate a nominal macromechanical *bridging zone strain* through the elastic correction of the recorded strain in a manner similar to that followed for the calculation of crack opening (Eq. (1)). This provides a basis for comparing the *macromechanical* against the *micromechanical* behavior, i.e. the recorded mechanical strain against the actual bridging strain obtained via LRM-probing of single bridging fibers.

Fig. 12 represents the macromechanically derived bridging stress as a function of nominal bridging strain obtained for a specimen of $t = 2\text{ mm}$ and $2\alpha_0/W = 0.5$. The testing procedure was interrupted at four displacement levels to allow for in situ LRM scanning along the bridging zone; the loci of the LRM measurements are demonstrated by the transient load relaxations corresponding to the cross-head extension-hold procedure. The strain values obtained at each step via the Raman microprobe are presented in Fig. 13. Strain tendency profiles along the ligament are provided by fitting the data with cubic spline regressions (solid lines). The dashed lines in Fig. 13 correspond to the upper standard deviation band of the measurements, a value obtained by the addition of one stan-

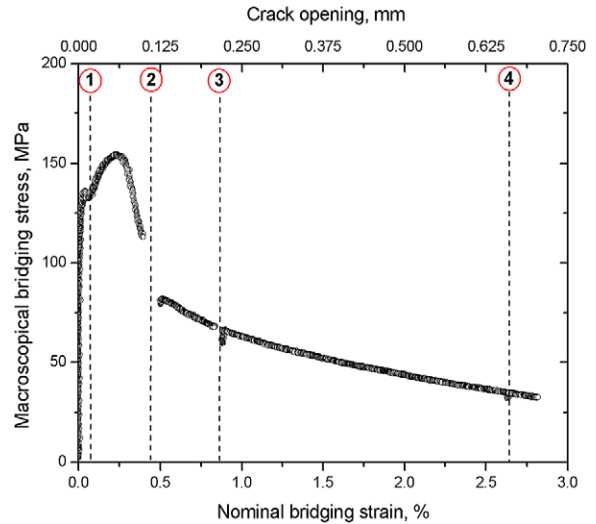


Fig. 12. Mechanical testing of SiC/MAS-L composite: Typical macromechanical behavior and loci of in situ LRM measurements (dashed lines, steps 1–4).

dard deviation to the mean fiber strain calculated at each acquisition step. It must be noted that the statistics performed at each acquisition step involved only the data in the range of 0.1–0.9 normalized position along the ligament (plateau data) and did not include the data with zero strain values (the significance of these values is discussed in the following). The scatter of multiple measurements performed on different locations along the same fiber falls within the standard deviation of the stress-free position of the 1350 cm^{-1} band (0.38 cm^{-1}) indicating that the strain is distributed uniformly along the scanned length of the fibers.

The first LRM-acquisition step (Fig. 13a) was performed at the onset of the fully developed macrocrack where the separation of the crack flanks was still small and all the fibers were still intact. At this stage, a few negative strain values were captured by the Raman microprobe. This compressive behavior of distinct fibers during the early fracture stages results from non-uniform load sharing between available fibers, a situation which arises from local microstructural imperfections and leaves certain filaments inactive and hence still subject to their residual strain state. In other words, the measured compressive strains stem from those fibers that have not yet assumed the externally

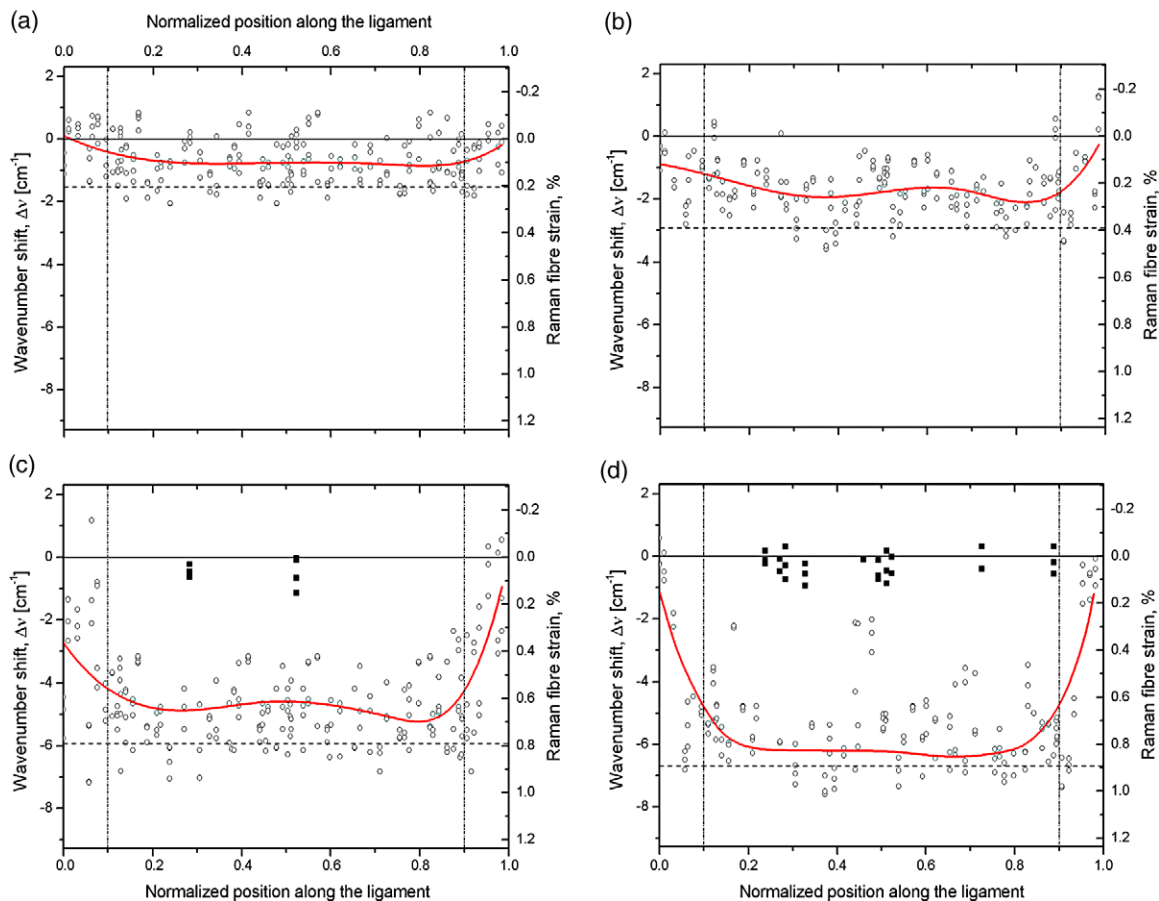


Fig. 13. (a)–(d). In situ LRM strain probing on bridging fibers in SiC/MAS-L composite ($t = 2$ mm, $2\alpha_0/W = 0.5$). Hollow circles represent results from individual fibers, solid squares represent load-free fibers, full lines are spline regressions to the data, whereas dashed lines correspond to the upper standard deviation band strain attained at each acquisition step. LRM strain remains uniform within a region of 0.1–0.9 normalized position along the ligament marked by dash-dot lines.

applied deformation and still carry the compressive strain due to fiber/matrix thermal expansion mismatch effects during composite fabrication. As discussed in [31], the difference between the thermal expansion coefficients of the matrix and the fiber in the longitudinal direction ($2.1 \times 10^{-6} \text{ }^\circ\text{C}^{-1}$ and $3.9 \times 10^{-6} \text{ }^\circ\text{C}^{-1}$, respectively) gives rise to residual thermal strains on the fibers of -0.18% in the longitudinal direction. In this study, the Raman probe captured residual strains of the order of ca. -0.13% . As the composite is loaded further, all the fibers assume the externally applied deformation and residual deformations merge in the total behavior. The second LRM-acquisition step

(Fig. 13b) corresponds to a composite state where a number of fibers have failed either within the matrix—resulting thus in a pull-out contribution—or between the crack flanks, leading to a mechanically inactive fiber with zero strain. The number of failed fibers increases successively in the third and fourth acquisition steps.

Information on the integrity of the fiber, as well as the type of failure that it has undergone (either within the matrix or along the exposed length), is provided by the magnitude of the LRM strain. Zero LRM strain values appearing with increasing frequency in the region 0.1–0.9 normalized position along the ligament at the third and fourth acqui-

sition steps correspond to fibers that are load free and do not contribute to the composite behavior. These fibers have failed either between the crack flanks or inside the matrix within short distances from the crack flank (small pull-out lengths) and have pull-out completely. In either case, 2% of the captured fibers within the bridging zone are load-free in the third step, whereas this percentage rises to 11% at the fourth step. Additionally, fibers with non-zero LRM strains that are lower than the spline-plateau value of the specific acquisition step correspond to those that have failed near the crack flank resulting in pull-out tractions that are lower than the tractions produced by fibers with higher pull-out lengths. By an examination of Fig. 13a–d, it is observed that fiber strain relaxes in the vicinity of the notch roots, more specifically within the regions of 0–0.1 and 0.9–1.0 normalized position along the ligament. This effect can be attributed to stress concentration gradients that develop locally around the notch tip and lead to premature fiber failures thus creating a “strain build-up” effect in the measured profiles. Strain is uniformly distributed along the region of 0.1–0.9 normalized position on the ligament.

A comparison between the macromechanical strain of the SiC/MAS-L composite and the strain of individual fibers within the bridging zone is presented in Fig. 14, where the spline-plateau strain (hollow circles) and upper standard deviation band strain (solid squares) on bridging fibers are plotted as a function of nominal macromechanical bridging zone strain for each LRM-acquisition step. The solid line represents the 1:1 behavior, whereas the dotted lines correspond to the typical error associated with the LRM measurements, equal to the standard deviation of the stress-free position of the 1350 cm^{-1} band. The x -axis values of Fig. 14 were obtained from the macromechanical bridging stress vs. nominal bridging strain curve (Fig. 12) as the abscissas corresponding to each LRM-acquisition step. Also plotted in both the axes of Fig. 14 is the specific fiber failure strain, $\epsilon_{failure} = 1.3\%$, observed during the calibration of the 1350 cm^{-1} band position with respect to the applied strain.

A close agreement between the macromechanical and LRM results is apparent for the first three

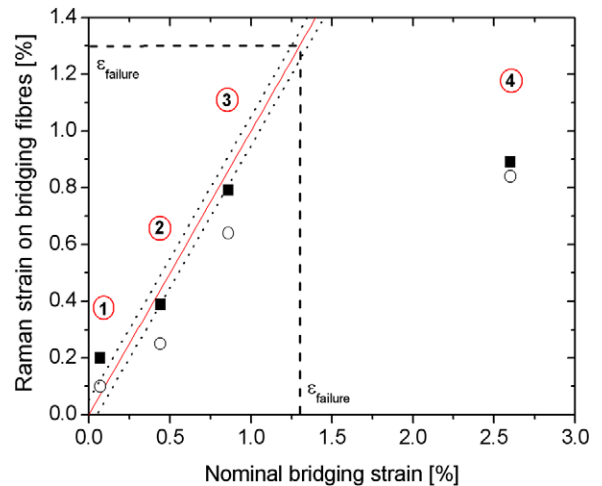


Fig. 14. Large scale bridging: Comparison of macromechanically derived results to actual behavior of fibers in the microscale.

acquisition steps in contrast to the last acquisition step where a wide divergence is noted. The observed behavior can be rationalized by considering the relative contributions of bridging due to intact fibers and that due to pull-out fibers: while most of the probed fibers are load-carrying up to the third acquisition step, the opposite holds for the fourth step where most of the fibers undergo pull-out. Hence, the nominal macromechanical bridging zone strain value of 2.6% attained at the fourth acquisition step does not correspond to the actual fiber elongation but only to the crack flank separation, constrained by friction at the fiber–matrix interface.

The upper standard deviation band of LRM strain reaches a saturation value of ca. 0.8% at the third acquisition step where the system transits to pure pull-out. This saturation effect is expected since the pull-out mechanism cannot lead to an increase in fiber strain. On the other hand, the fact that the upper standard deviation band of fiber strain measured within the macrocrack is 38% less than the fiber failure strain (1.3%) in conjunction with the observation that the majority of fibers fails within their embedded length (evidenced by the small number of zero-strain fibers at the fourth acquisition step) leads to the conclusion that the failure scenario of fibers in the composite is greatly

different to that of free-standing fibers. While the latter tend to fail solely due to their surface flaw distribution, the failure of fibers embedded in the composite seems to be strongly affected also by fiber/matrix interactions as, for example, friction along the interface. This observation is, in practical terms, an experimental demonstration of the weakest link statistics that govern the failure of fiber-reinforced brittle-matrix composites.

A measure of the bridging stress carried by intact and pull-out fibers can be obtained by multiplying the measured Raman strains with the fibers' elastic modulus, 220 GPa. The stress values corresponding to the upper standard deviation bands for the 4 LRM-acquisition steps are in increasing step order: 440, 850, 1738 and 1958 GPa, respectively. These values are much higher than the macromechanical bridging stresses of 133, 100, 66 and 34 MPa calculated as the ordinates corresponding to each LRM-acquisition step in Fig. 12. The difference is inherent to the procedure used for the determination of macromechanical bridging stress where the composite is treated as a closed system—neglecting even the volume fraction of the fibers in the composite—and, hence, fails to distinguish between the contributions of failed and intact fibers. In fact, similar to a fiber bundle test, the decreasing part in the load–displacement curve (Fig. 5) after the maximum load corresponds to a decrease in composite strength due to incremental fiber failure. On the other hand, the LRM technique can distinguish between the fibers that have survived and those that have failed between the crack flanks. The non-zero LRM strains measured in this study originate from individual fibers which have not failed between the crack flanks. These fibers behave linear elastically up to failure and carry a monotonically increasing load during the tensile test. It is still, however, questionable whether LRM can independently distinguish between the intact fibers and the fibers that undergo pull-out. The answer to this question is currently under investigation and will, hopefully, be dealt with in a future publication.

6. Conclusions

In this study, the LRM technique was applied for direct in situ quantification of strains acting on distinct bridging fibers during the monotonic tensile loading of a SiC/MAS-L composite with intense LSB characteristics. Using a newly developed ultra-high precision remote Raman microscope integrated with a mechanical testing frame, bridging strain profiles were calculated at four different loading stages during composite fracture by scanning the bridging zone along the notched ligament of the specimen with the Raman microprobe. The established profiles exhibited a strain plateau spanning 80% of the ligament in symmetric distances from the notch root, while they indicated a strain build-up effect in the vicinity of the notch root. The Raman strains were compared to the nominal values of macromechanical bridging zone strain calculated through an elastic correction approach of the measured strain. Within the Weibull fiber failure regime, measured strains were in good agreement with the macromechanical bridging strain of the composite proving that, following the development of a dominant macrocrack, the composite fracture is governed by independent fiber action and incremental fiber failure. In accordance with the weakest link statistical nature of fracture governing the Class I composite of this study, the plateau value of the measured strains was less than the fiber failure strain indicating that the fiber failures occur mostly along their embedded length at locations dictated by their specific surface flaw distribution.

Acknowledgements

The authors wish to thank Mr. Patrick Peres of EADS (France) for providing the composite material used in this study. The valuable assistance of Mr. Christos Koimtzoglou and Dr. John Parthenios of ICE/HT-Forth (Hellas) in crucial experimental issues concerning mechanical testing and spectroscopic measurements respectively, is gratefully acknowledged.

References

- [1] Evans AG, Zok FW. *J. Mater. Sci.* 1994;29:3857.
- [2] Cox BN. *Acta Mater.* 1991;39:1189.
- [3] Fett T, Munz D, Geraghty RD, White KW. *Eng. Fract. Mech.* 2000;66:375.
- [4] Foote RML, Mai Y-W, Cotterell B. *J. Mech. Phys. Solids* 1986;34:593.
- [5] Hu XZ, Mai YW. *J. Mater. Sci.* 1992;27:3502.
- [6] Fett T, Munz D. *J. Eur. Ceram. Soc.* 1995;15:337.
- [7] Cao JW, Sakai M. *Carbon* 1996;34:387.
- [8] Kostopoulos V, Markopoulos YP. *Mat. Sci. Eng. A-Struct.* 1998;250:303.
- [9] Sorensen BF, Jacobsen TK. *Compos. Part A-Appl. S.* 1998;29:1443.
- [10] Rausch G, Kuntz M, Gratwohl G. *J. Am. Ceram. Soc.* 2000;84:2762.
- [11] Jacobsen TK, Sorensen BF. *Compos. Part A-Appl. S.* 2001;32:1.
- [12] Brenet P, Conchin F, Fantozzi G, Reynaud P, Rouby D, Tallaron C. *Compos. Sci. Technol.* 1996;84:817.
- [13] Galiotis C. *Compos. Sci. Technol.* 1991;42:125.
- [14] Marston C, Galiotis C. *J. Mater. Sci.* 1998;33:5311.
- [15] Filiou C, Galiotis C. *Compos. Sci. Technol.* 1999;59:2149.
- [16] Koimtzoglou C, Kostopoulos V, Galiotis C. *Compos. Part A-Appl. S.* 2001;32:457.
- [17] Arjyal BP, Galiotis C, Ogin SL, Whittingham RD. *Compos. Part A-Appl. S.* 1998;29:1363.
- [18] Bennet JA, Young RJ. *Compos. Part A-Appl. S.* 1998;29:1071.
- [19] Parthenios J, Katerelos DG, Psarras GC, Galiotis C. *Eng. Fract. Mech.* 2002;69:1067.
- [20] Bollet F, Galiotis C, Reece MJ. *Composites* 1996;27:729.
- [21] Marshall DB, Cox BN. *Acta Mater.* 1985;33:2013.
- [22] Kostopoulos V, Markopoulos YP, Pappas YZ, Peteves SD. *J. Eur. Ceram. Soc.* 1997;18:69.
- [23] Dassios KG, Kostopoulos V, Steen M., *Compos Sci Technol* 2003. [in press].
- [24] Cox BN, Marshall DB, Thouless MD. *Acta Mater.* 1989;37:1933.
- [25] Sutcu M. *Acta Mater.* 1989;37:651.
- [26] Curtin WA. *J. Am. Ceram. Soc.* 1991;74:2837.
- [27] Thouless MD, Evans AG. *Acta Metall Mater* 1988;3:517.
- [28] Llorca J, Elices M. *Acta Metall. Mater.* 1990;12:2485.
- [29] Simon G, Bunsell AR. *J. Mater. Sci.* 1984;19:3649.
- [30] Wu HF, Netravali AN. *J. Mater. Sci.* 1992;27:3318.
- [31] Drissi-Habti M. *J. Eur. Ceram. Soc.* 1997;17:22.